



Decoration of MnO Nanocrystals on Flexible Freestanding Carbon Nanofibers for Lithium Ion Battery Anodes



Edmund Samuel^{a,1}, Hong Seok Jo^{a,1}, Bhavana Joshi^a, Seongpil An^a, Hyun Goo Park^a, Yong Il Kim^a, Woo Young Yoon^{b,*}, Sam S. Yoon^{a,*}

^aSchool of Mechanical Engineering, Korea University, Seoul 02481, Republic of Korea

^bDepartment of Materials Science & Engineering, Korea University, Seoul 02841, Republic of Korea

ARTICLE INFO

Article history:

Received 3 January 2017

Accepted 14 February 2017

Available online 16 February 2017

Keywords:

Electrospun nanofiber

MnO

Freestanding

Flexible

Carbon nanofiber

Lithium battery anode

ABSTRACT

We demonstrate the fabrication of freestanding and flexible MnO-decorated carbon nanofiber (CNF) composites as lithium-ion battery anode materials. They showed an initial capacity of 1131 mAh·g⁻¹ and a retention capacity of 923 mAh·g⁻¹ after 90 charge–discharge cycles under a current rate of 123 mA·g⁻¹. Decoration of MnO nanocrystals on the CNFs enhanced the lithium storage capacity of the composites. The optimal concentration of MnO was identified by varying its weight percentage from 0 to 7%. When the concentration was increased, more reaction sites for lithium ions were formed, which in turn increased the overall specific capacity. The intensity of the *D* band in the Raman spectra of the decorated CNFs was higher than that of the *G* band, indicating the enhanced diffusion of lithium ions. The plateau region of the discharge curve observed in the cases of higher MnO concentrations indicated the active reduction of MnO; consequently, a higher reversible capacity was achieved. These flexible and freestanding MnO–CNF nanocomposites can be used in lightweight, portable, and flexible batteries.

© 2017 Elsevier Ltd. All rights reserved.

1. Introduction

Lithium-ion batteries (LIBs) are the most promising power sources for portable electronic devices because they offer high specific capacity and long cycle life [1]. The commercial LIB anode material of graphite has a low specific capacity (theoretically 372 mAh·g⁻¹) and suffers poor rate capability [2]. Therefore, the requirement of high anode capacity at higher current rates and long cycle life has stimulated significant research focused on improving the performance of anode materials for LIBs. High-capacity anode materials of transition metal oxide (TMO) composites have great potential in electric vehicles and hybrid electric vehicles because of their abundant raw materials, low cost, and environmental benignity [2,3].

Co₃O₄, MnO, and SnO₂ have very high theoretical capacities of 890, 755, and 781 mAh·g⁻¹, respectively, [4–6] and several advantages over graphite anodes, such as widespread availability, good stability, and efficient charge transfer because of their various oxidation states [7]. Thus, TMOs show immense prospective

benefits as anode materials. Among TMOs, MnO shows significant potential because of its abundant availability, non-toxicity [8], low conversion potential (<0.8 V) [3,9,10], and environmental friendliness [11]. However, volume changes (or expansion) of MnO occurs, as in other metal oxides, during lithiation; contraction during delithiation can cause the pulverization of the electrode, which leads to a rapid decay in capacity. MnO also suffers from poor electrical conductivity and therefore it requires improvement to achieve high stability and specific capacity.

These major concerns of MnO in LIB applications can be alleviated by utilizing carbon nanofibers. The electrical conductivity of MnO/CNF composites is higher than that of the binary oxide (MnO) alone because of the presence of the CNFs. The porous natures of CNFs provide space for the volume change of the MnO during lithiation and delithiation. The formation of Li dendrites is lessened because of the large CNF surface area, which provides sufficient active sites for Li ion electrochemical reactions [2,12,13]. In addition, the nanoscale nature of CNF shortens the ionic diffusion distance required for rapid kinetic reactions, which enhances the LIB performance.

Qiu et al. added nitrogen to MnO/carbon nanocomposites by a facile decomposition method to improve the conductivity [14]. Sun et al. used multi-walled carbon nanotubes (MWCNTs) with MnO to generate a conducting network [15]. However, the random

* Corresponding authors.

E-mail addresses: wyyoon@korea.ac.kr (W.Y. Yoon), skyoonyoon@korea.ac.kr, skyoonsoyoung@gmail.com (S.S. Yoon).

¹ These authors have contributed equally.

distribution of MWCNT and their sintering approach prevented reaching a sufficiently high capacity, and they were not able to test the materials under high current rates [15]. Ji et al. [16] first utilized CNFs to accommodate MnO for LIB applications. Liu et al. [11] and Wang et al. [2] also used MnO/CNFs as anodes in LIBs. None of these MnO/CNF composites was flexible, which is important for use in portable flexible electronics. Most of these studied materials were not freestanding, necessitating the use of heavy current collectors that hinder the mobility of batteries in hybrid vehicles and portable electronics.

Herein, we demonstrate excellent LIB anode performance using flexible and freestanding MnO/CNF composites. The CNF is decorated with MnO, which increases the electrical conductivity and surface area while offering good mechanical strength. Freestanding and flexible properties are facilitated for lightweight and convenient use. The optimal MnO decoration was sought to yield the best LIB performance, for which the MnO weight concentration was varied from 0 to 7%. The highly conductive CNF and composites thereof work as current collectors, enabling the development of ultra-thin LIBs.

2. Experimental

2.1. Freestanding flexible MnO mats

Electrospinning was employed to fabricate CNF and MnO/CNF composite mats, as shown schematically in Fig. 1a. Polyacrylonitrile (PAN, $M_w = 150$ kDa, Sigma-Aldrich) was mixed at 8 wt% with *N,N*-dimethylformamide (DMF, 99.8%, Sigma-Aldrich) to prepare a homogeneous polymer solution, as reported in our earlier work [17]. Different amounts of manganese acetate ($\text{Mn}(\text{CH}_3\text{COO})_2$, or MnAc), as shown in Table 1, were added to the above PAN/DMF solution and stirred for 20 min. The solution was used as a precursor and loaded into a syringe pump for electrospinning at the high voltage of 9–10 kV for 90 min and a flow rate of $500 \mu\text{L} \cdot \text{h}^{-1}$. A needle-to-collector (Al foil) distance of 15 cm was employed to ensure stable electrospinning. The obtained mats are pale orange in color (Fig. 1b), before being stabilized at 280°C for 30 min in N_2 . After stabilizing the composite mats, the samples were peeled off from the Al foil collector and carbonized at 700°C in Ar at the temperature ramping rate of $3^\circ\text{C} \cdot \text{min}^{-1}$. The carbonized

Table 1
Precursor composition.

Case No.	MnAc (wt%)
1	0
2	2
3	5
4	7

mats are highly flexible, as shown in Fig. 1c, and are used directly by punching them for the LIB electrode.

2.2. Electrochemical tests

Electrochemical tests were conducted on coin-type CR2032 half-cells of CNF and CNF/MnO composites as anode materials for LIBs. The LIB battery performances were measured for Cases 1–4, and each anode had a circular area of 1.54 cm^2 . A metallic Li sheet was used as the reference electrode in a half-cell constructed in a dry room. A microporous polyethylene film (Celgard 2400; Celgard, South Korea) was used as the separator between the two electrodes. The electrolyte was 1 M LiPF_6 in a solvent mixture of ethylene carbonate (EC), dimethylcarbonate (DMC), and ethyl methyl carbonate (EMC) (1:1:1 by volume) (PuriELSOulbrain, Seongnam, South Korea). Galvanostatic discharge/charge curves were measured at 25°C using a WBCS3000 battery cycler system (WonATech, South Korea). The cells were subjected to current rate performance tests at current rates of 123, 246, 616, and $1232 \text{ mA} \cdot \text{g}^{-1}$. The current rate was decreased from 1232 to $123 \text{ mA} \cdot \text{g}^{-1}$ and for each current rate, the test was performed for 5 cycles to demonstrate the rate capability of our MnO/CNF composite for low to high current rates.

3. Results and Discussion

X-ray diffraction (XRD, SmartLab, Rigaku) patterns obtained from the CNFs and MnO/CNFs are shown in Fig. 2a. The diffraction peak of the CNFs at 21° indicates the (120) plane of the graphite-like layers in the fiber. In Case 2, the peak at 21° shows higher intensity than the other peaks of MnO because of the relatively low concentration of MnO. The presence of MnO is confirmed from the

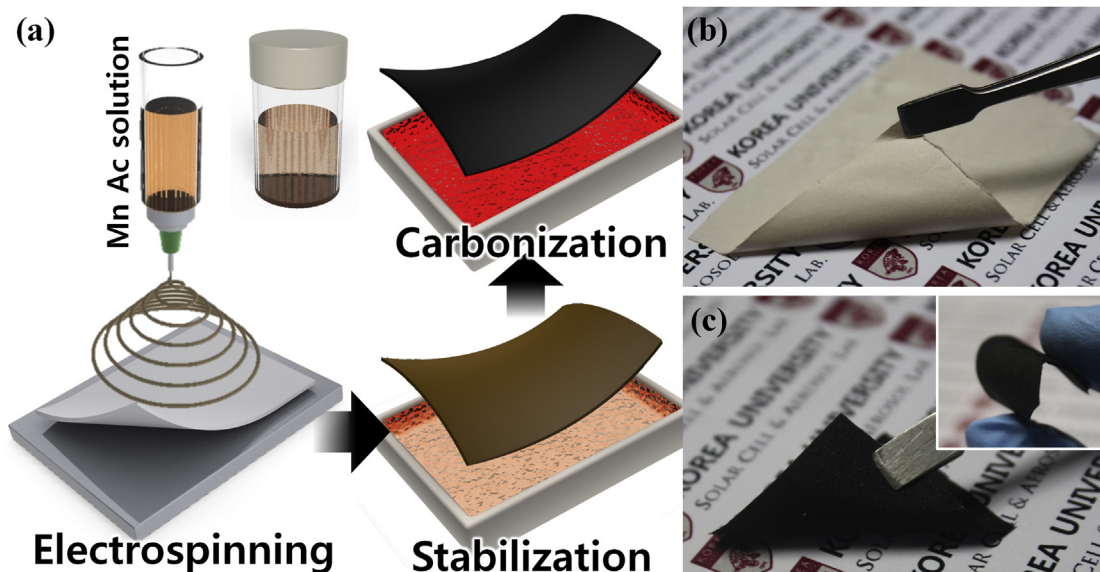


Fig. 1. Schematics showing steps to obtain freestanding flexible NF mat: (a) electrospinning process, stabilization under N_2 at 280°C for 30 min, and carbonization under Ar gas at 700°C for 2 h. Photographs of (b) as-deposited pale orange-colored mat, (c) carbonized freestanding mat with (inset) good flexibility.

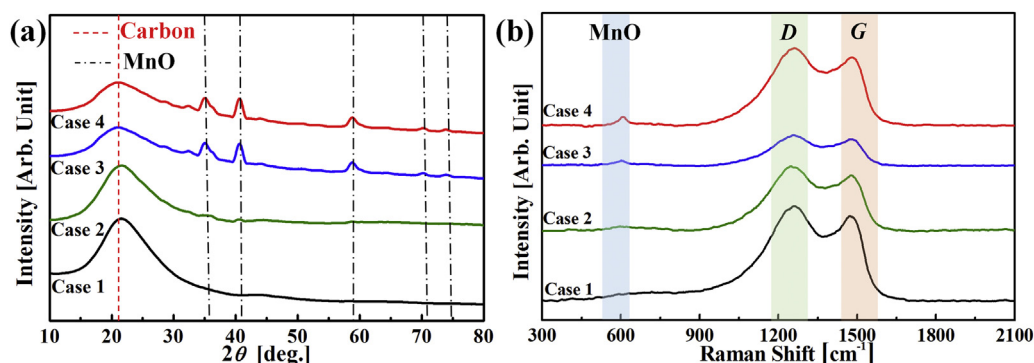


Fig. 2. (a) XRD patterns and (b) Raman Spectra of freestanding MnO/CNF composites (Cases 1–4).

diffraction peaks at $2\theta = 36.2^\circ$ (111), 40.6° (200), 58.8° (220), 70.4° (311), and 73.6° (222) for Cases 2–4. The diffraction peaks show the cubic phase of MnO, matched with JCPDS cards 78-0424 [4] and 07-0230 [5]. From the peaks and full width at half maximum (FWHM) of the MnO/CNF composites made with 2, 5, and 7 wt% of MnAc, the average crystal sizes of 1, 8.6, and 8.8 nm are calculated using the Scherrer equation $D = K\lambda/\beta\cos\theta$. Here, D is the crystallite size (nm), K is Scherrer constant (0.9), λ is the X-ray wavelength for Cu $K\alpha$ radiation (0.154 nm), β is the FWHM of the peaks shown in Fig. 2a for Cases 2–4, and θ is the angle of the diffraction peak. Several MnO nanocrystallites present on the surface of the CNF generate a unique phase, which leads to kinetically stabilized MnO/CNF composites [2,18,19].

Raman spectra (HORIBA JOBIN YVON, LabRam ARAMIS IR2) were used to study the structural changes of the carbon nanofibers for Cases 1–4, as shown in Fig. 2b. The peaks at 1474 and 1254 cm^{-1} correspond to the G and D bands, related to sp^2 carbon bond stretching and defects, respectively [11,20]. The peaks at 1483 , 1478 , 1476 , and 1474 cm^{-1} for the different cases are attributed to the E_{2g} mode (in-plane vibration) of sp^2 -bonded carbon atoms [21]. The D band peaks for Cases 1–4 at 1260 , 1258 , 1255 , and 1254 cm^{-1} , respectively, are related to the Raman inactive A_{1g} vibration mode and structural disorder from lattice distortion [22]. The intensity ratio of the D and G bands, or I_D/I_G , presented in Table 2, shows an increase from 1.04 to 1.13 with the embedding of MnO in the CNFs for Cases 1–4 (in Case 1, the MnO wt.% is 0). The higher I_D/I_G value suggests more defects in the CNF, which contribute to the improved diffusion of Li ions and provide more intercalation sites for storing Li ions [11]. Moreover, the higher intensity of the D band indicates better Li-ion storage performance [11]. I_D/I_G values greater than unity indicate the completely crystalline state of both C and MnO, with no amorphous nature. Additionally, no peaks originate at 644 cm^{-1} or below 400 cm^{-1} , suggesting the formation of highly stable MnO/CNF composites without Mn_3O_4 [22,23]. The MnO peaks for Cases 2–4 are present at the low-frequency end of the Raman spectra in the radial breathing-mode band at 593 , 599 , and 608 cm^{-1} , respectively. The intensity of the MnO peaks is lower than that of the D and G bands because of the low concentration of MnO relative to C in the composites.

Table 2
D and G band peak positions and its intensity ratio.

Case	D peak [cm^{-1}]	G peak [cm^{-1}]	I_D/I_G	MnO peak [cm^{-1}]
1	1260	1483	1.04	–
2	1258	1478	1.03	593
3	1255	1476	1.07	599
4	1254	1474	1.13	608

The elemental and electronic surface states were analyzed by using X-ray photoelectron spectroscopy (XPS, X-TOOL, ULVAC-PHI) on Case 4 specimens, with results shown in Fig. 3. The binding energies of C 1s and O 1s indicated by the peaks obtained through the scanned spectra are 284.75 and 530.75 eV , respectively. The deconvoluted strong peak of C 1s at 284.75 eV corresponds to the C–C bonds in the CNF of the composite. The other three peaks at 284 , 285.25 , and 286 eV , corresponding to C=C, C=O, and C–O, respectively, may be related to the functional groups and residues of C bonded with O from an incomplete reduction [24]. The Mn $2p_{1/2}$ and Mn $2p_{3/2}$ peaks at 653.75 and 641.5 eV , respectively, show the characteristics of MnO [11]. The spin orbit splitting between Mn $2p_{1/2}$ and Mn $2p_{3/2}$ is $\sim 11.75 \text{ eV}$, confirming the crystallization of MnO. The binding energy peak at 641.5 eV , corresponding to Mn $2p_{3/2}$, indicates that the Mn is in the Mn^{2+} state. Furthermore, the binding energy peak at 530.75 eV in Fig. 3d indicates that O is present in the O^{2-} state.

Investigation of the morphological details of the MnO/CNF composites was performed by transmission electron microscopy (TEM, JEM 2100F, JEOL Inc.). The TEM image at low magnification in Fig. 4a shows the uniform embedding of MnO throughout the CNF. The detailed structural study, expanded for the optimized loading amount of MnO (7 wt%) in Case 4 using TEM, shows embedded MnO particles of a few nanometers in size on the CNF. The circle in Fig. 4a indicates the area observed by selected-area electron diffraction (SAED), shown in the inset. The SAED pattern of the MnO nanoparticle reveals discrete spots, suggesting a nanocrystalline phase of MnO. The lattice fringes in Fig. 4b confirm the interplanar spacings of 0.22 nm and 0.25 nm for the (200) and (111) planes of the cubic MnO phase. The elemental maps of C, Mn, and O are shown in Fig. 4c.

Fig. 5 shows the discharge and charge profiles, which provide insights on the Li-ion insertion/extraction phenomenon and the Mn phase changes. The CNF/MnO composite mats were directly used as freestanding and flexible anodes for the LIBs to investigate their Li-ion storage characteristics. The specific capacities were calculated based on the weight of the entire composite specimens. Fig. 5 shows the discharge/charge profiles obtained at a current rate of $123 \text{ mA}\cdot\text{g}^{-1}$ for Cases 1–4. The lithiation/delithiation occurred in the voltage range of 0.01 – 3.0 V and the number of cycles N are 1, 2, and 90. In the discharge/charge curves for Cases 1–4, voltage drops of ~ 0.75 , 0.83 , 0.72 , and 0.7 V , respectively, occur during $N = 1$; at this voltage, a plateau region appears. The plateau region in the discharge curve indicates where a consistent increase in capacity occurs with minor voltage variations. Thus, with a minor decrease in voltage, the discharge of the battery increases along with the capacitance, in accordance with the anode material's morphology. The increase in capacitance and prolonged discharge duration is attributed to the phase change of Mn^{2+} to Mn^0 and the formation of LiO_2 . However, at $N = 2$, no plateau

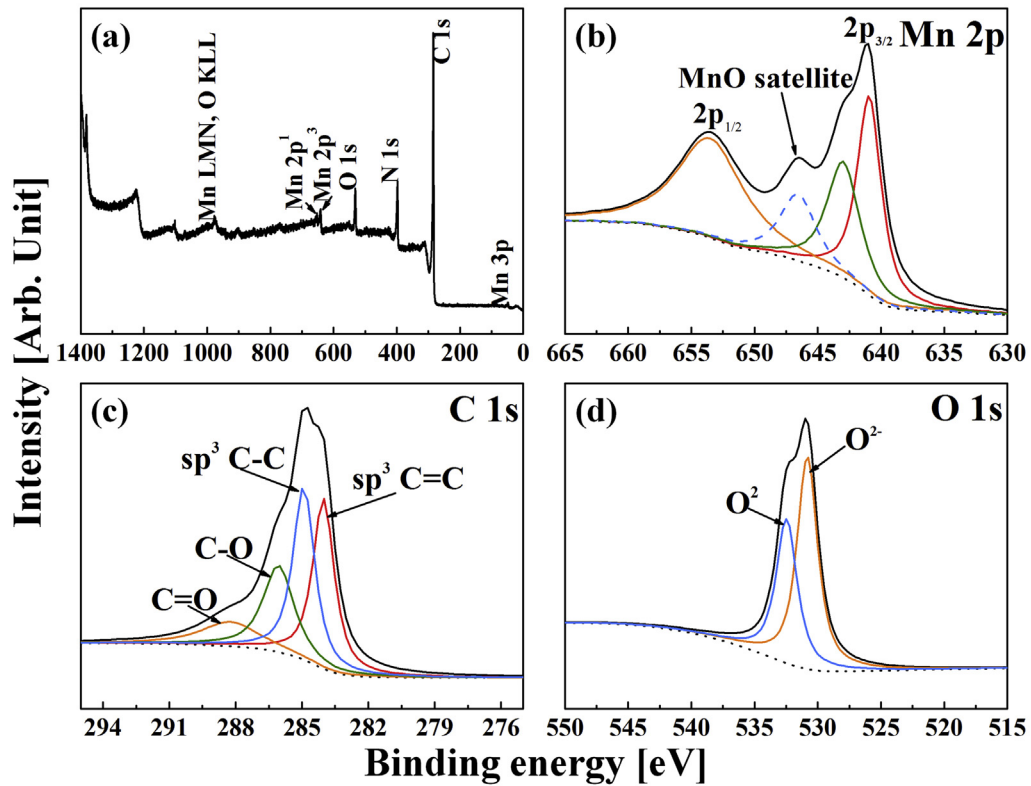


Fig. 3. High-resolution XPS spectra of MnO/CNF (Case 4): (a) Survey, (b) Mn 2p (c) C 1s, and (d) O 1s orbitals.

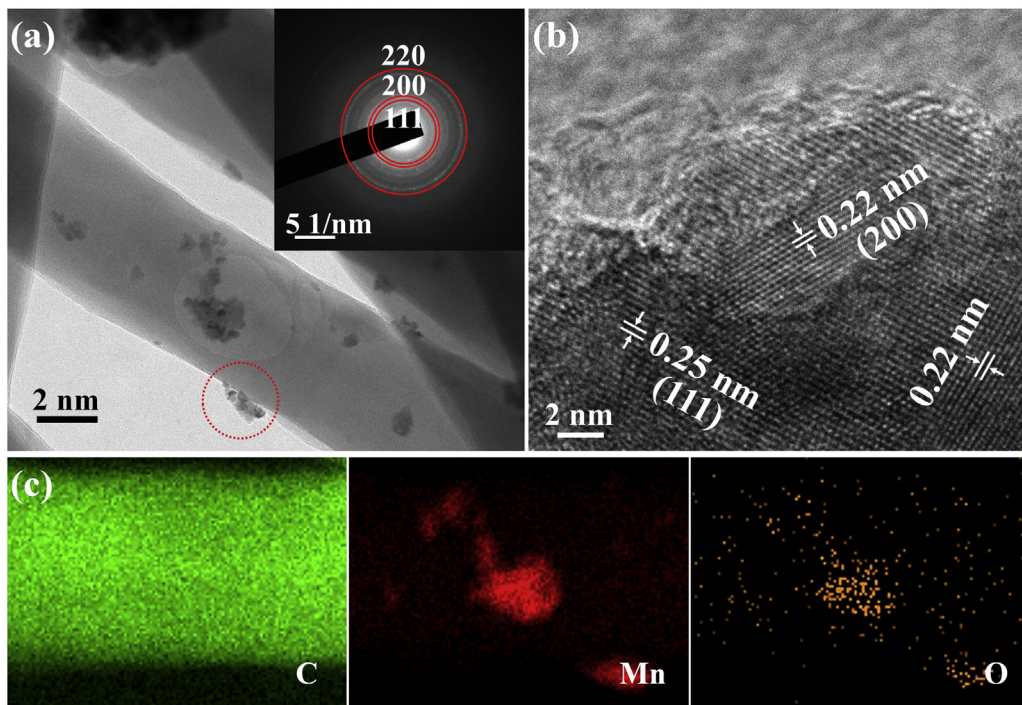


Fig. 4. TEM image of MnO/CNF composite of Case 4 flexible fiber. (a) embedded MnO on CNF, with SAED pattern in inset, (b) HR-TEM image, (c) elemental maps of C, Mn, and O.

occurs; instead, a gradual decrease in voltage appears. Furthermore, the curves of Cases 3 and 4 around 0.28 and 0.25 V, respectively, show elongated horizontal second plateau regions during lithiation. The elongated plateau regions for Cases 3 and 4

are near the plateau potential of MnO (where the operating potential is 0.2 V vs Li^+/Li), indicating the high concentration of MnO in the MnO/CNF composites [3]. During lithiation, MnO is converted to metallic-phase Mn^{2+} and Mn^{3+} [25]. Furthermore, in

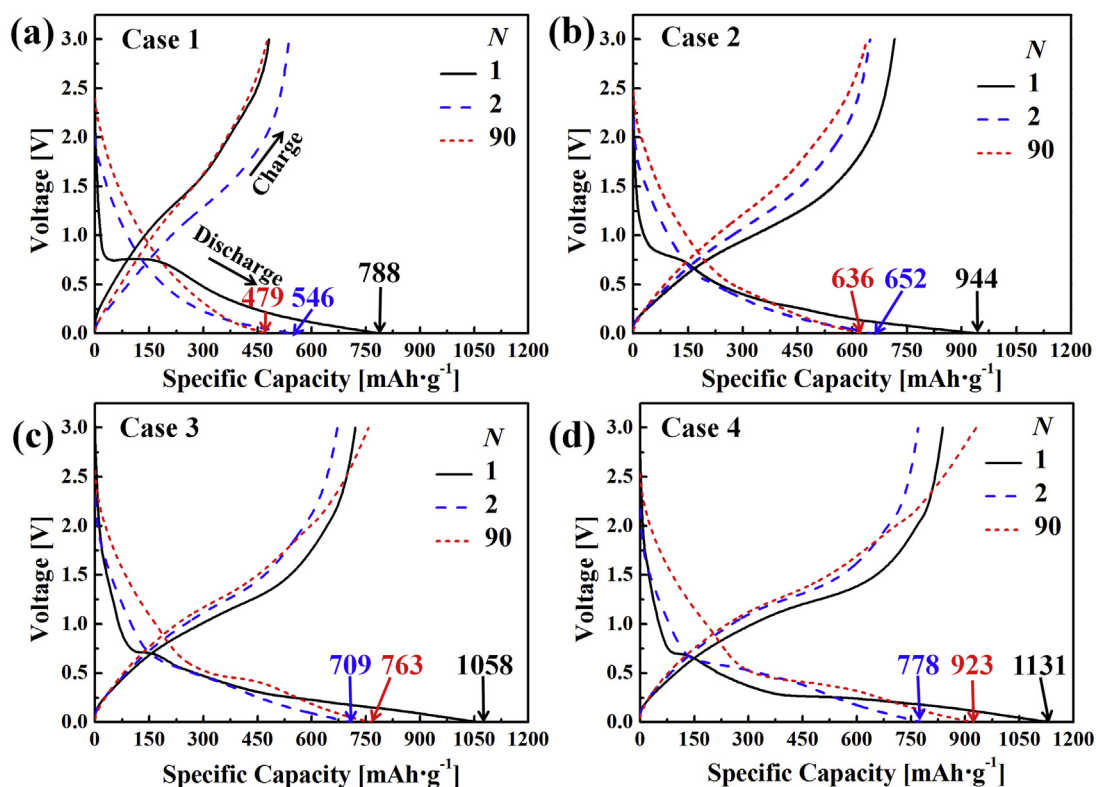
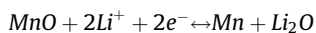


Fig. 5. Charge/discharge curves for MnO/CNF (Cases 1–4) at $123 \text{ mA}\cdot\text{g}^{-1}$.

Fig. 5, the charging (delithiation) profile for Case 4 shows the slope width of 1.03 V with a voltage ranging from 0.7–1.73 V. This is associated with the oxidation of Mn^0 to Mn^{2+} [25]. During the discharge process, Mn^{2+} is converted to Mn^0 . Conversely, during the charge process, Mn^0 is converted to Mn^{2+} . These conversions occur by the following reaction:



The specific discharge capacities of the LIBs for Cases 1–4 at $N=1$ are 788, 944, 1058, and 1131 $\text{mAh}\cdot\text{g}^{-1}$, respectively. The corresponding Coulombic efficiencies for $N=1$ are 61, 76, 68, and 64% for Cases 1–4, respectively. Here, the Coulombic efficiency is deduced from the ratio of capacity obtained for delithiation and lithiation in each cycle. The Coulombic efficiency is lower in value because irreversible capacitance loss occurs during discharging when $N=1$, attributed to the formation of the solid electrolyte interface (SEI) layer. Further, the Coulombic efficiencies of Cases 1–4 are increased to 98, 99, 95, and 99%, respectively, at $N=2$, which is attributed to the completion of SEI layer formation and the enhancement of the reversible capacitance [26–28]. The Coulombic efficiency increases to >99% at $N=90$ for Cases 1–4. Notably, the MnO particles provide additional active sites to Li ions with their decoration on the CNFs, as depicted in Fig. 4a [29].

In addition to the superior capacity, the freestanding MnO/CNF anode presents good cycling performance at different current densities. The electrodes were tested for different current densities ranging from 123 to $1232 \text{ mA}\cdot\text{g}^{-1}$ for all cases. As shown in Fig. 6, the pristine CNF and MnO/CNF composites exhibit excellent performance and restoration of battery capacity. The first $N=1$ capacities for Cases 1–4 at the current rate of $123 \text{ mA}\cdot\text{g}^{-1}$ are 788, 944, 1058, and 1131 $\text{mAh}\cdot\text{g}^{-1}$, respectively. The corresponding first reversible discharge capacities are 546, 652, 709, and 778 $\text{mAh}\cdot\text{g}^{-1}$. The current rate is increased to $1232 \text{ mA}\cdot\text{g}^{-1}$, which introduces significant polarization at the interface of the electrolyte and

electrode; hence, the overall capacity drops. Once the applied high current rate ($1232 \text{ mA}\cdot\text{g}^{-1}$) is decreased back to $123 \text{ mA}\cdot\text{g}^{-1}$ at $N=31$, all cases regain specific capacity values close to those recorded at $N=5$, indicating the stability of all cases for a wide range of current rates. It is observed from Cases 3 and 4 that the capacity retention is higher for sufficient loading of MnO. The capacity restoration percentages for the MnO/CNF composites (Cases 1–4) are 61, 67, 72, and 82% at $N=90$ (cycles), respectively. A vast decline in specific capacity is observed for Case 1 from $N=2$ to 90 in the absence of MnO, from 546 to 479 $\text{mAh}\cdot\text{g}^{-1}$. For Case 4, when MnO has the highest loading of 7 wt%, a significant increment of specific capacity occurs from 778 to 923 $\text{mAh}\cdot\text{g}^{-1}$. This is because the agglomerated or larger MnO particles break into smaller domains under the stress developed from the continuous

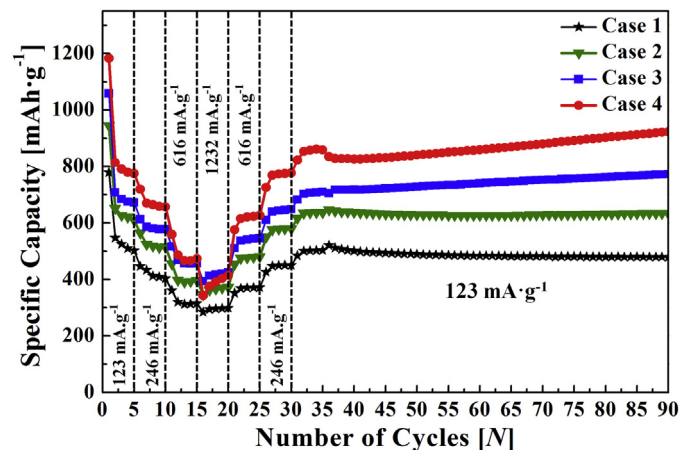


Fig. 6. Cycling performance at different current rates for Cases 1–4 ($N=1$ –30) and long cycling performance at $123 \text{ mA}\cdot\text{g}^{-1}$ ($N=31$ –90) with the voltage range of 0.01–3.0 V.

Table 3

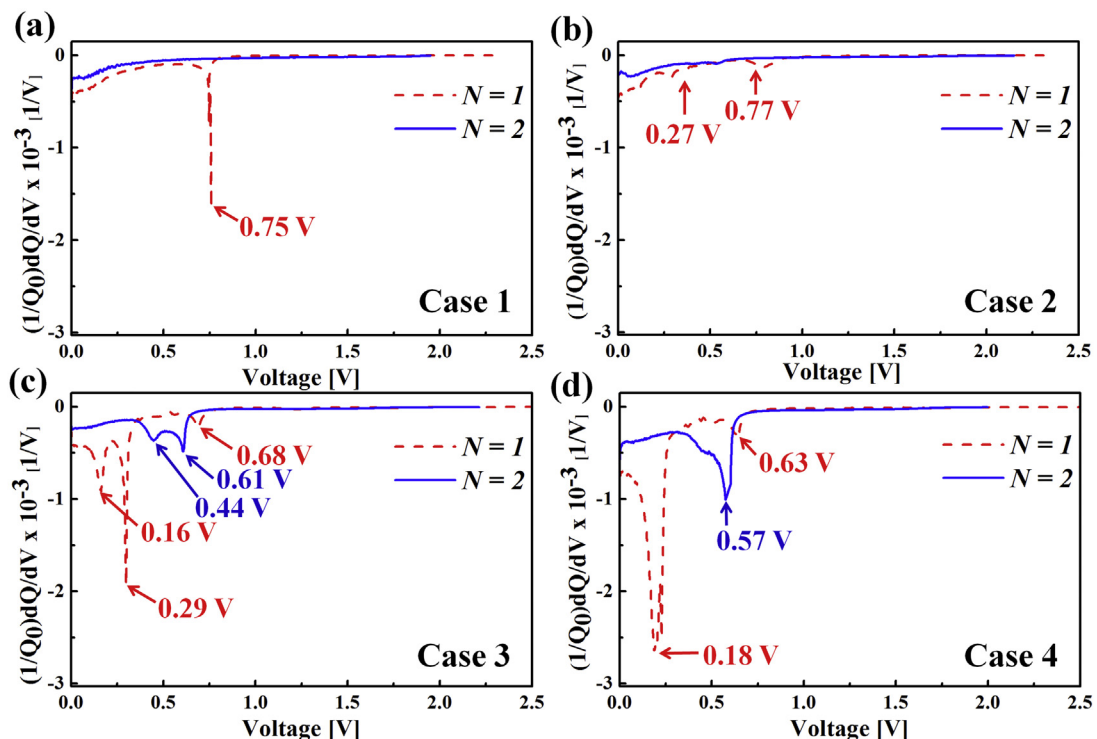
Comparison of the specific capacity of the present film with literature values.

Composition	Electrode prepared	Free-standing/ Flexibility	First Discharge capacity [$\text{mAh}\cdot\text{g}^{-1}$]	First reversible capacity [$\text{mAh}\cdot\text{g}^{-1}$]	Capacity retention [$\text{mAh}\cdot\text{g}^{-1}$](N^{th})	Current rate [$\text{mA}\cdot\text{g}^{-1}$]	Refs.
MnO/CNF	Nanofiber	No/No	1155	785	597(50)	50	[16]
MnO/rGO	Nanoparticles w/binder	No/No	1001	647	665(50)	100	[20]
MnO/MWNT	Hydrothermal (rods)	No/No	1050	710	690(5)	14	[15]
MnO/CB	Microspheres w/binder	No/No	1010	767	625(60)	100	[30]
MnO/CB	Thermal decomposing w/binder	No/No	931	570	473(50)	100	[14]
MnO/CNF	Nanofibers	No/No	1350	900	850(80)	100	[11]
MnO/CNF	Nanofibers	Yes/No	1021	663	557(50)	50	[2]
MnO/Carbon	Nanoparticles w/ binder	No/No	1490	799	578(60)	100	[31]
MnO/CNF	Nanofibers (flexible)	Yes/Yes	1131	778	923(90)	123	Present

expansion and contraction in the volume of the MnO. Thus, the smaller domains contribute additional increases in the surface area, which decreases the diffusion path length for Li-ions and increases the capacity in return. However, in the absence of MnO, the possibility of any additional increment in surface area does not exist; on the contrary, the existing Li-ion host sites are consistently blocked by SEI layers. The capacity retention values mentioned by the works referenced in Table 3 vary from 38–66%. Comparatively, a better retention capacity is obtained by our Case 4 (82%, for $N=90$). Furthermore, in Case 4 of this work, the applied current density was $123 \text{ mA}\cdot\text{g}^{-1}$, which is a higher current loading than that applied to the cases listed in Table 3. Thus, our MnO/CNF not only demonstrates better flexibility in Fig. 1c, but also shows

consistent and better performance than other composite anode materials.

The highest capacity retention of Case 4 is from the optimal concentration of MnO nanocrystals and CNF, which yields a hybrid nanostructure showing synergetic effects of MnO and CNF. In Fig. 4 a, the uniform embedding of nano-crystalline MnO on the CNF and voids between individual CNFs are shown. This provides enhanced numbers of active sites via the large surface area, which also accommodates the volume expansion. Although the anodes were tested at a very high current rate ($1232 \text{ mA}\cdot\text{g}^{-1}$) the MnO endured the battery performance with the support of CNF. Therefore, we extended our study to demonstrate long cycling performance (at the current rate of $123 \text{ mA}\cdot\text{g}^{-1}$) for Cases 1–4 in a continuation of the current rate cycles. The composites showed overall excellent

Fig. 7. Differential capacitance curves for $N=1$ and 2 of Case 1–4.

performance with higher Coulombic efficiency (>99%) and stability. However, Case 4 shows an especially high capability to recover capacity losses among the tested cases. The enhancement in the specific capacity retention confirms the excellent reversible reaction during lithiation/delithiation process of the MnO/CNF composite electrodes.

The long cycle performance after operating in high-current-rate conditions and the retention of capacity for the current rate of 123.2 mA·g⁻¹ are both excellent. Thus, the strategical optimization of the binder-free and conductive active material provided very high battery capacity (923 mAh·g⁻¹) under a high current rate as well as after very long cycling ($N=90$), as observed in Fig. 6.

The electrochemical behavior and its analysis were extended by studying the differential capacitance across the discharging voltages, as shown in Fig. 7 for Cases 1–4. During the first discharging cycle for Case 1, almost no variation occurs until a sharp reduction peak appears at 0.75 V, corresponding to the formation of SEI layers. However, from the second cycle onward, no reduction peak is observed, indicating stable SEI layer formation during the first cycle. Moreover, the absence of any other peaks indicates that only CNF provides active sites to the Li ions, with no morphological changes. In contrast to the pristine CNF (Case 1), the MnO/CNF composite shows multiple peaks for Case 2 at 0.27 and 0.77 V. However, for Case 3, prominent peaks are observed during $N=1$ at 0.16, 0.29, and 0.68 V. At $N=2$, two prominent peaks remain, although the shifts in position (0.44 and 0.61 V) and decreased intensity indicate that the SEI layer formation process was completed during $N=1$ itself. The shift in the peaks during the second cycle indicates an irreversible reduction reaction and textural alterations during lithiation/delithiation (conversion mechanism process) [32]. Here, the peaks at 0.16 and 0.29 V correspond to the reduction of Mn²⁺ and Mn³⁺ to Mn⁰ and SEI layer formation, respectively [8]. Fig. 7d shows for Case 4 two peaks during $N=1$, present at 0.18 and 0.63 V, related to SEI layer formation and Li-ion insertion. When $N=2$, the SEI layer stabilizes and no additional peaks are observed. The shift in peak location is attributed to the reversible phase transformation resulting from the formation of metallic Mn by reduction and the formation of Li₂O [31].

4. Conclusion

We have successfully synthesized MnO/CNF composites by electrospinning in a one-step process that is adaptable for large and industrial scale production. The structural characterization and composition analysis explained the excellent behavior of MnO/CNF as an anode material. The electrochemical tests indicated that our composites provided high reversible capacity. Thus, the unique synergy of MnO and CNF creates an encouraging anode candidate for LIBs.

Acknowledgements

This work was supported by the Industrial Strategic Technology Development Program (10045221) funded by the Ministry of Knowledge Economy (MKE, Korea) and by Global Frontier Program through the Global Frontier Hybrid Interface Materials (GFHIM) of NRF-2013M3A6B1078879.

References

- [1] F. Gao, J.-y. Qu, Z.-b. Zhao, Y.-f. Dong, J. Yang, Q. Dong, J.-s. Qiu, Easy synthesis of MnO-graphene hybrids for high-performance lithium storage, *New Carbon Materials* 29 (4) (2014) 316–321.
- [2] J.-G. Wang, Y. Yang, Z.-H. Huang, F. Kang, MnO-carbon hybrid nanofiber composites as superior anode materials for lithium-ion batteries, *Electrochimica Acta* 170 (2015) 164–170.
- [3] Y. Deng, L. Wan, Y. Xie, X. Qin, G. Chen, Recent advances in Mn-based oxides as anode materials for lithium ion batteries, *RSC Advances* 4 (45) (2014) 23914.
- [4] K. Zhong, X. Xia, B. Zhang, H. Li, Z. Wang, L. Chen, MnO powder as anode active materials for lithium ion batteries, *Journal of Power Sources* 195 (10) (2010) 3300–3308.
- [5] Q. Hao, L. Xu, G. Li, Z. Ju, C. sun, H. Ma, Y. Qian, Synthesis of MnO/C composites through a solid state reaction and their transformation into MnO₂ nanorods, *Journal of Alloys and Compounds* 509 (21) (2011) 6217–6221.
- [6] G.L. Xu, Y.F. Xu, J.C. Fang, F. Fu, H. Sun, L. Huang, S. Yang, S.G. Sun, Facile synthesis of hierarchical micro/nanostructured MnO material and its excellent lithium storage property and high performance as anode in a MnO/LiNi_{0.5}Mn_{1.5}O(4- δ) lithium ion battery, *ACS applied materials & interfaces* 5 (13) (2013) 6316–6323.
- [7] W. Li, G. Li, J. Sun, R. Zou, K. Xu, Y. Sun, Z. Chen, J. Yang, J. Hu, Hierarchical heterostructures of MnO(2) nanosheets or nanorods grown on Au-coated Co(3)O(4) porous nanowalls for high-performance pseudocapacitance, *Nanoscale* 5 (7) (2013) 2901–2908.
- [8] C. Chae, J.H. Kim, J.M. Kim, Y.-K. Sun, J.K. Lee, Highly reversible conversion-capacity of MnO-loaded ordered mesoporous carbon nanorods for lithium-ion battery anodes, *Journal of Materials Chemistry* 22 (34) (2012) 17870.
- [9] M. Srivastava, J. Singh, T. Kuila, R.K. Layek, N.H. Kim, J.H. Lee, Recent advances in graphene and its metal-oxide hybrid nanostructures for lithium-ion batteries, *Nanoscale* 7 (11) (2015) 4820–4868.
- [10] Hao Jiang, Y.H. Shaojun Guo, Chaoyi Yan, Pooi See Lee, Chunzhong Li, Rational Design of MnO/Carbon Nanopeapods with Internal Void Space for High-Rate and Long-Life Li-Ion Batteries, *ACS Nano* 8 (2014) 6038–6046.
- [11] B. Liu, X. Hu, H. Xu, W. Luo, Y. Sun, Y. Huang, Encapsulation of MnO nanocrystals in electrospun carbon nanofibers as high-performance anode materials for lithium-ion batteries, *Scientific reports* 4 (2014) 4229.
- [12] L. Ji, Z. Lin, M. Alcoutlabi, X. Zhang, Recent developments in nanostructured anode materials for rechargeable lithium-ion batteries, *Energy & Environmental Science* 4 (8) (2011) 2682.
- [13] Lili Feng, Z.X. Hongbo Zhao, Yang Bai, Junming Guo, Chang-wei Su, Xiaokai Chen, MnO₂ prepared by hydrothermal method and electrochemical performance as anode for lithium-ion battery, *Nanoscale Research Letters* 9 (2014) 1–8.
- [14] S. Qiu, X. Wang, G. Lu, J. Liu, C. He, Facile synthesis of MnO and nitrogen-doped carbon nanocomposites as anode material for lithium ion battery, *Materials Letters* 136 (2014) 289–291.
- [15] X. Sun, Y. Xu, P. Ding, M. Jia, G. Ceder, The composite rods of MnO and multi-walled carbon nanotubes as anode materials for lithium ion batteries, *Journal of Power Sources* 244 (2013) 690–694.
- [16] L. Ji, A.J. Medford, X. Zhang, Porous carbon nanofibers loaded with manganese oxide particles: Formation mechanism and electrochemical performance as energy-storage materials, *Journal of Materials Chemistry* 19 (31) (2009) 5593.
- [17] B.N. Joshi, S. An, H.S. Jo, K.Y. Song, H.G. Park, S. Hwang, S.S. Al-Deyab, W.Y. Yoon, S.S. Yoon, Flexible, Freestanding, and Binder-free SnO(x)-ZnO/Carbon Nanofiber Composites for Lithium Ion Battery Anodes, *ACS applied materials & interfaces* 8 (14) (2016) 9446–9453.
- [18] R. Tsybukh, A comparative study of platinum nanodeposits on HOPG (0001), MnO (100) and MnOx/MnO (100) surfaces by STM and AFM after heat treatment in UHV, O₂, CO and H₂, Leiden Institute of Chemistry, CASC, Faculty of Science, Leiden University, 2010.
- [19] Z. Lin, L. Ji, M.D. Woodroof, X. Zhang, Electrodeposited MnOx/carbon nanofiber composites for use as anode materials in rechargeable lithium-ion batteries, *Journal of Power Sources* 195 (15) (2010) 5025–5031.
- [20] Y.J. Mai, D. Zhang, Y.Q. Qiao, C.D. Gu, X.L. Wang, J.P. Tu, MnO/reduced graphene oxide sheet hybrid as an anode for Li-ion batteries with enhanced lithium storage performance, *Journal of Power Sources* 216 (2012) 201–207.
- [21] Q. Sun, Z. Wang, Z. Zhang, Q. Yu, Y. Qu, J. Zhang, Y. Yu, B. Xiang, Rational Design of Graphene-Reinforced MnO Nanowires with Enhanced Electrochemical Performance for Li-Ion Batteries, *ACS applied materials & interfaces* 8 (10) (2016) 6303–6308.
- [22] W. Zhu, H. Huang, W. Zhang, X. Tao, Y. Gan, Y. Xia, H. Yang, X. Guo, Synthesis of MnO/C composites derived from pollen template for advanced lithium-ion batteries, *Electrochimica Acta* 152 (2015) 286–293.
- [23] X. Li, Y. Zhu, X. Zhang, J. Liang, Y. Qian, MnO@1-D carbon composites from the precursor C₄H₄MnO₆ and their high-performance in lithium batteries, *RSC Advances* 3 (25) (2013) 10001.
- [24] Y. Sun, X. Hu, W. Luo, Y. Huang, Porous carbon-modified MnO disks prepared by a microwave-polyol process and their superior lithium-ion storage properties, *Journal of Materials Chemistry* 22 (36) (2012) 19190.
- [25] Z. Cui, X. Guo, H. Li, High performance MnO thin-film anodes grown by radio-frequency sputtering for lithium ion batteries, *Journal of Power Sources* 244 (2013) 731–735.
- [26] L.H. Huang, Z.H. Min, Q.Y. Zhang, Solid electrolyte inter-phase on graphite anodes in Li-ion batteries, *Rev Adv. Mater. Sci* 36 (2014) 13–20.
- [27] M.B. Pinson, M.Z. Bazant, Theory of SEI Formation in Rechargeable Batteries: Capacity Fade, Accelerated Aging and Lifetime Prediction, *Journal of the Electrochemical Society* 160 (2) (2012) A243–A250.
- [28] A.L. Lipson, K. Puntambekar, D.J. Comstock, X. Meng, M.L. Geier, J.W. Elam, M.C. Hersam, Nanoscale Investigation of Solid Electrolyte Interphase Inhibition on Li-Ion Battery MnO Electrodes via Atomic Layer Deposition of Al₂O₃, *Chemistry of Materials* 26 (2) (2014) 935–940.

- [29] C.-T. Hsieh, C.-Y. Lin, J.-Y. Lin, High reversibility of Li intercalation and de-intercalation in MnO-attached graphene anodes for Li-ion batteries, *Electrochimica Acta* 56 (24) (2011) 8861–8867.
- [30] X. Wang, S. Qiu, G. Lu, C. He, J. Liu, L. Luan, W. Liu, Fabrication of porous MnO microspheres with carbon coating for lithium ion battery application, *CrystEngComm* 16 (9) (2014) 1802.
- [31] H. Liu, Z. Li, Y. Liang, R. Fu, D. Wu, Facile synthesis of MnO multi-core@nitrogen-doped carbon shell nanoparticles for high performance lithium-ion battery anodes, *Carbon* 84 (2015) 419–425.
- [32] X. Cui, Y. Wang, Z. Chen, H. Zhou, Q. Xu, P. Sun, J. Zhou, L. Xia, Y. Sun, Y. Lu, Preparation of pompon-like MnO/carbon nanotube composite microspheres as anodes for lithium ion batteries, *Electrochimica Acta* 180 (2015) 858–865.